Halo formation in three-dimensional bunches

R. L. Gluckstern and A. V. Fedotov
Physics Department, University of Maryland, College Park, Maryland 20742

S. Kurennoy and R. Ryne
Los Alamos Neutron Science Center Division, Los Alamos National Laboratory, Los Alamos, New Mexico 87545

(Received 7 April 1998)

We have constructed, analytically and numerically, a class of self-consistent six-dimensional (6D) phase space stationary distributions. Stationary distributions allow us to study the halo development mechanism without it being obscured by beam redistribution and its effect on halo formation. The beam is then mismatched longitudinally and/or transversely, and we explore the formation of longitudinal and transverse halos in 3D axisymmetric beam bunches. We find that the longitudinal halo forms first for comparable longitudinal and transverse mismatches because the longitudinal tune depression is more severe than the transverse one for elongated bunches. Of particular importance is the result that, due to the coupling between longitudinal and transverse motion, a longitudinal or transverse halo is observed for a mismatch less than 10% if the mismatch in the other plane is large. [S1063-651X(98)05410-5]

PACS number(s): 29.27.Bd, 41.85.Ew

I. INTRODUCTION

The need for high current in a variety of new accelerator applications has focused a great deal of attention on understanding the phenomenon of halo formation in ion beams, which can cause excessive radioactivation of the accelerator. Starting in about 1991, a variety of two-dimensional (2D) simulation studies [1,2] have led to the conclusion that halos are formed when a beam is mismatched to a focusing channel, exciting some sort of collective oscillation(s) of the beam that are in resonance with the nonlinear oscillation of individual ions.

Most of the simulations studies start with rms matched beams that are *not* stationary solutions of the Vlasov equation (See, for example, [3]). As a result, the initial beam undergoes some sort of redistribution in phase space, masking the possible development of halos. Our effort has been devoted to populating a stationary distribution in phase space, in the hope that the halo development mechanism can be studied without being obscured by the ''relaxation'' of the beam in phase space. We have particularly studied initial distributions that are stationary by virtue of being a function only of the Hamiltonian.

Our first analysis [2] started with an azimuthally symmetric KV [4] beam where the 4D phase space distribution function was a δ function of the Hamiltonian of the form

$$f(H)=N\delta(H-H_0). \tag{1.1}$$

We assume that the transverse focusing force is independent of longitudinal position (AG forces are smoothed). The Hamiltonian is written as

$$H=\frac{kr^2}{2}+e\Phi_{sc}(r)+\frac{mv^2}{2}, \tag{1.2}$$

where $\Phi_{sc}(r)$ is the electrostatic space charge potential, and where N is a normalization constant chosen so that

$$\int d\boldsymbol{v}\int d\boldsymbol{r}\, f(H)=1. \tag{1.3}$$

By starting with the envelope equation for a breathing 2D beam in real space, we were able to treat analytically the parametric resonance between the breathing mode and the nonlinear motion of an individual ion the amplitude of which is greater than the core radius [2]. The resulting phase space consists of an inner separatrix containing the core and an outer separatrix that becomes the locus near which the halo particles enter and cluster. Numerical simulations starting with a ''breathing'' KV beam confirm the analytic prediction of the ''peanut-shaped'' 4D phase space, showing clearly the dominant behavior of the parametric resonance. A typical example is shown in Fig. 1 for a mismatch (ratio of initial beam radius to matched beam radius) of 0.7 and a tune de-

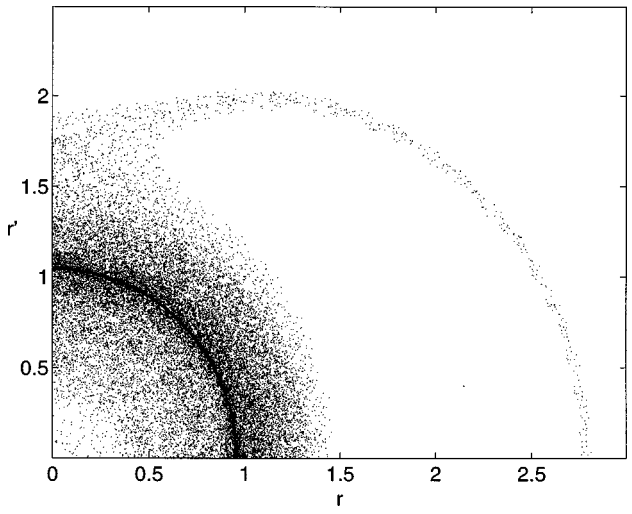

FIG. 1. Typical stroboscopic plot in the transverse phase space for 125 particles with low angular momenta for a KV beam ($\eta=0.8$, $\mu=0.7$).

pression (ratio of small amplitude ion oscillation frequency with space charge to that without space charge) of 0.8 [5].

The parametric resonance model successfully predicts the location of the halo, but it gives no information about the rate at which the halo develops or the fraction of the ions in the core that enter the halo. Nevertheless, simulations provide evidence that the fraction of the ions that enter the halo is surprisingly insensitive to the tune depression but increases strongly as the mismatch becomes more severe [5]. In addition, the motion starts to show chaotic behavior for tune depressions of 0.5 and below, a feature not addressed by the analytic model.

A further shortcoming of the analytic model is that it did not explain how ions were able to leave the core. This, however, was subsequently explained by an analytic treatment of the stability of a breathing KV beam [6], which accurately predicted the regions in the mismatch–tune depression space where oscillation modes were unstable. Simulations starting with a breathing KV beam confirmed that these instabilities led to oscillation amplitude growth, with ions often entering the outer separatrix region, corresponding to halo formation, for sufficiently large mismatch [5,6].

Finally we considered other 4D stationary distributions of the form

$$f(H)=\begin{cases} N(H_0-H)^{n-1}, & H\leqslant H_0 \\ 0, & H\geqslant H_0, \end{cases} \tag{1.4}$$

with $n=1$ (water bag) and $n=2$ [7]. We were unable to explore the effect of the parametric resonance analytically, but numerical simulations showed the development of halos very similar to those for the KV distribution. Specifically, phase space again consisted of a ''peanut diagram,'' with parameters close to those for the KV distribution. As with a KV beam, it became clear that instabilities in the ''breathing mode'' allowed ions to enter a region where the parametric resonance enabled them to move across the inner separatrix. The only significant change from the KV simulations was that comparable halo formation required more severe mismatches than before.

To summarize, we believe, from the analytic treatment of the breathing KV beam and the simulations of the KV and other stationary distributions, that instabilities in the breathing beam allow particles to repopulate the 4D phase space in a way that allows the parametric resonance to generate halos.

Finally, it is clear that a realistic treatment of halo formation must take into account 3D beam bunches and 6D phase space distributions. Recently, Barnard and Lund [8] performed numerical studies with a 3D beam bunch using the particle-core model, drawing attention to the existence and importance of a longitudinal halo for a spheroidal bunch. However, all studies based on the particle-core model do not address the question of whether halo formation is influenced by the density redistribution that follows for a nonstationary beam, even if it is rms matched [3]. In fact, halo formation in 2D due to the redistribution process in rms matched beams was shown, for example, by Okamoto [9] and Jameson [10]. We therefore continue our effort to study the halo development mechanism in 3D beam bunches in the absence of the redistribution process. Such an approach allows us to study the fundamental mechanism of halo formation associated with the beam mismatch. This method proved to be very efficient in previous 2D calculations [5–7]. To accomplish this we have constructed, analytically and numerically, a new class of stationary 6D phase space distributions for a spheroidal beam bunch. Our present analysis assumes smoothed external transverse and longitudinal restoring force gradients, k_z, k_y, k_x. In general, the distribution can be chosen to have an approximately ellipsoidal boundary. However, for simplicity, we treat the azimuthally symmetric case ($k_x = k_y$) for which the beam bunch is approximately spheroidal. This is the focus of the present investigation.

II. STATIONARY 6D PHASE SPACE DISTRIBUTION

A. Distribution and charge density

We take for the azimuthally symmetric 6D phase space distribution

$$f(\boldsymbol{x},\boldsymbol{p})=N(H_0-H)^{-1/2}, \tag{2.1}$$

where

$$H=k_x r^2/2+k_z z^2/2+e\Phi_{sc}(\boldsymbol{x})+mv^2/2. \tag{2.2}$$

Here $\boldsymbol{p}=m\boldsymbol{v}$, $r^2=x^2+y^2$, and k_x, k_z are the smoothed transverse and longitudinal restoring force gradients. The quantity $\Phi_{sc}(\boldsymbol{x})$ is the electrostatic potential due to the space charge of the bunch. The distribution is normalized such that

$$\int d\boldsymbol{x}\int d\boldsymbol{p} f(\boldsymbol{x},\boldsymbol{p})=1. \tag{2.3}$$

The charge distribution corresponding to Eq. (2.1) is

$$\rho(\boldsymbol{x})=Q\int d\boldsymbol{p} f(\boldsymbol{x},\boldsymbol{p})=NQm^3\int d\boldsymbol{v}\left[G(\boldsymbol{x})-\frac{mv^2}{2}\right]^{-1/2}, \tag{2.4}$$

where

$$G(\boldsymbol{x})\equiv H_0-\frac{k_x r^2}{2}-\frac{k_z z^2}{2}-e\Phi_{sc}(\boldsymbol{x}). \tag{2.5}$$

Performing the integral over $d\boldsymbol{v}\equiv v^2 dv\, d\Omega_v$ in Eq. (2.4) leads to

$$\rho(\boldsymbol{x})=QG(\boldsymbol{x})\Big/\int d\boldsymbol{x} G(\boldsymbol{x}), \tag{2.6}$$

where the normalization constant satisfies

$$2\sqrt{2}\pi^2 Nm^{3/2}\int d\boldsymbol{x} G(\boldsymbol{x})=1. \tag{2.7}$$

From Eq. (2.5) and Poisson's equation, we write

$$\nabla^2 G(\boldsymbol{x})=-k_s-e\nabla^2\Phi_{sc}=-k_s+(e/\epsilon_0)\rho(\boldsymbol{x}), \tag{2.8}$$

where

$$k_s=2k_x+k_z. \tag{2.9}$$

Using Eq. (2.6), we obtain the partial differential equation for $G(\boldsymbol{x})$,

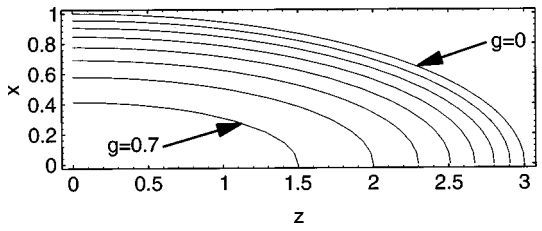

FIG. 2. Contours $g(\boldsymbol{x})=$const for $c/a=3$, $\eta_x=0.65$, $\eta_z=0.49$.

$$\nabla^2 G(\boldsymbol{x}) = -k_s + \kappa^2 G(\boldsymbol{x}), \tag{2.10}$$

where

$$\kappa^2 = (eQ/\epsilon_0) \Big/ \int d\boldsymbol{x} G(\boldsymbol{x}). \tag{2.11}$$

The solution of Eq. (2.10) for an axisymmetric, spheroidal shaped bunch can most easily be written in the spherical coordinates R, θ for which

$$z = R\cos\theta, \quad r = R\sin\theta, \tag{2.12}$$

as

$$G(\boldsymbol{x}) = (k_s/\kappa^2) g(\boldsymbol{x}), \tag{2.13}$$

where

$$g(\boldsymbol{x}) = 1 + \sum_{\ell=0}^{\infty} \alpha_\ell P_{2\ell}(\cos\theta) i_{2\ell}(\kappa R). \tag{2.14}$$

Here $P_{2\ell}(\cos\theta)$ are the even (fore-aft symmetric) Legendre polynomials and $i_{2\ell}(\kappa R)$ are the spherical Bessel functions (regular at $\kappa R=0$) of the imaginary argument.

Since $g(\boldsymbol{x})$ is proportional to the charge density, the edge of the bunch is defined as the border $g(\boldsymbol{x})=0$, closest to the origin. We therefore choose the α_ℓ's so that the surface of the bunch reproduces, as closely as possible, the ellipsoidal surface

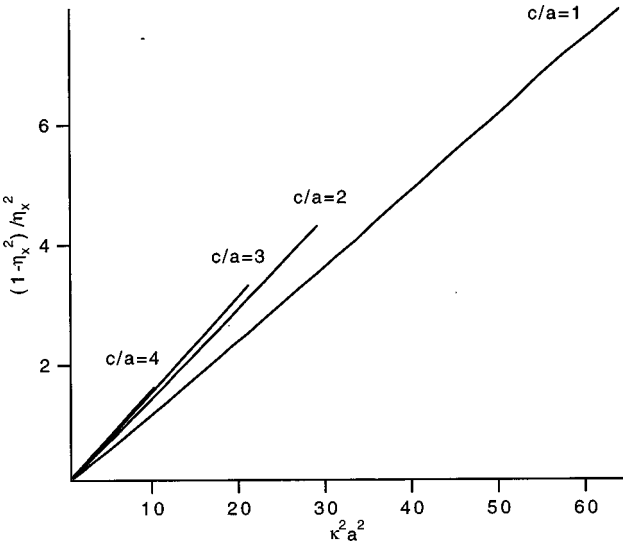

FIG. 3. $(1-\eta_x^2)/\eta_x^2$ vs $\kappa^2 a^2$ for different c/a.

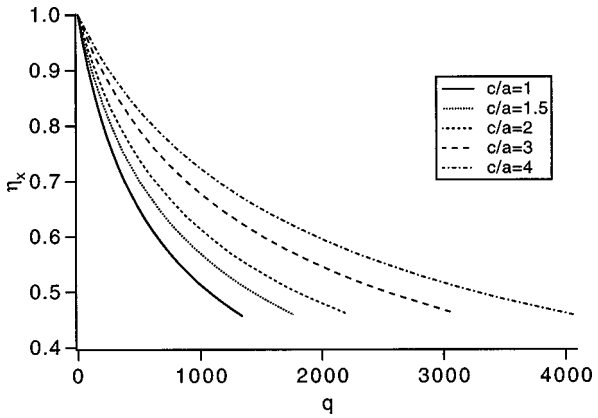

FIG. 4. Transverse tune depression η_x vs bunch charge.

$$\frac{r^2}{a^2} + \frac{z^2}{c^2} = 1, \quad R^2 = \left(\frac{\sin^2\theta}{a^2} + \frac{\cos^2\theta}{c^2} \right)^{-1}. \tag{2.15}$$

B. rms tune depressions and normalized emittance

The equations of motion for an individual ion are

$$m\ddot{x} = -k_x x + eE_x(\boldsymbol{x}) \tag{2.16}$$

and

$$m\ddot{z} = -k_z z + eE_z(\boldsymbol{x}), \tag{2.17}$$

where

$$\boldsymbol{E}(\boldsymbol{x}) = -\nabla\Phi_{sc}(\boldsymbol{x}). \tag{2.18}$$

Since the phase space distribution is a function only of the Hamiltonian H, it is stationary and satisfies

$$\sum_{i=1}^{3} \dot{x}_i \frac{\partial f}{\partial x_i} + \sum_{i=1}^{3} \ddot{x}_i \frac{\partial f}{\partial \dot{x}_i} = 0. \tag{2.19}$$

Multiplying Eq. (2.19) by $m x_j \dot{x}_j$ and integrating over $d\boldsymbol{x}\, d\dot{\boldsymbol{x}}$ leads, after integration by parts, to

$$m\langle \dot{x}_j^2 \rangle + \langle m\ddot{x}_j x_j \rangle = 0, \tag{2.20}$$

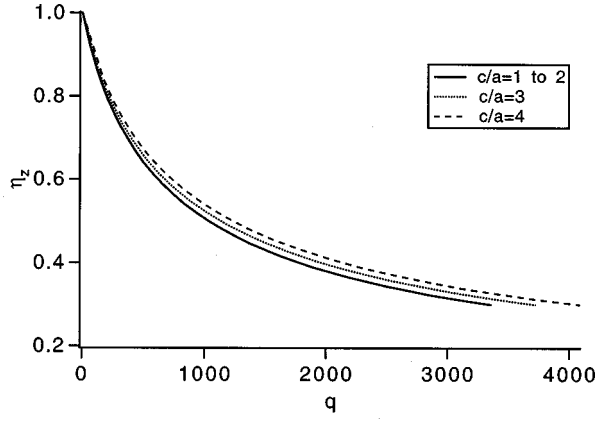

FIG. 5. Longitudinal tune depression η_z vs bunch charge.

TABLE I. ''Transverse breathing'' oscillations.

c/a	$\left(\frac{w_{\max}}{u_{\max}}\right)_{\text{analytic}}$	$\left(\frac{w_{\max}}{u_{\max}}\right)_{\text{numerical}}$
2	0.20	0.20 ± 0.04
3	0.14	0.15 ± 0.03
4	0.11	0.17 ± 0.02
5	0.08	0.17 ± 0.02

where $\langle\ \rangle$ stands for the average over the 6D phase space distribution. Using Eqs. (2.16) and (2.17) leads to

$$k_x\langle x^2\rangle - e\langle xE_x\rangle = m\langle \dot{x}^2\rangle, \tag{2.21}$$

$$k_z\langle z^2\rangle - e\langle zE_z\rangle = m\langle \dot{z}^2\rangle. \tag{2.22}$$

We note that the normalized emittance [11] has the form

$$\epsilon_x^2 = \langle \dot{x}^2\rangle\langle x^2\rangle/c_0^2, \quad \epsilon_z^2 = \langle \dot{z}^2\rangle\langle z^2\rangle/c_0^2, \tag{2.23}$$

in the absence of directional correlations between $\boldsymbol{x}$ and $\dot{\boldsymbol{x}}$, where c_0 is the velocity of light. Equations (2.21) and (2.22) play the role of rms envelope equations, allowing us to define the rms tune depression as

$$\eta_{x,\text{rms}}^2 \equiv \frac{m\langle \dot{x}^2\rangle}{k_x\langle x^2\rangle}, \quad \eta_{z,\text{rms}}^2 \equiv \frac{m\langle \dot{z}^2\rangle}{k_z\langle z^2\rangle}, \tag{2.24}$$

$$1-\eta_{x,\text{rms}}^2 = \frac{e\langle xE_x\rangle}{k_x\langle x^2\rangle}, \quad 1-\eta_{z,\text{rms}}^2 = \frac{e\langle zE_z\rangle}{k_z\langle z^2\rangle}, \tag{2.25}$$

or

$$\frac{1-\eta_x^2}{\eta_x^2} = \frac{e\langle xE_x\rangle}{m\langle \dot{x}^2\rangle}, \quad \frac{1-\eta_z^2}{\eta_z^2} = \frac{e\langle zE_z\rangle}{m\langle \dot{z}^2\rangle}. \tag{2.26}$$

We also note that $m\langle \dot{x}^2\rangle = m\langle \dot{y}^2\rangle = m\langle \dot{z}^2\rangle = m\langle v^2\rangle/3$ because H depends only on v^2 and $\boldsymbol{x}$. Thus our choice of a stationary distribution of the form $f(H)$ *automatically* corresponds to equipartition (equal average kinetic energy in the three spatial directions). We find $m\langle v^2\rangle$ by writing

$$\langle mv^2\rangle = \frac{\int d\boldsymbol{x}\int d\boldsymbol{v} mv^2[G(\boldsymbol{x})-mv^2/2]^{-1/2}}{\int d\boldsymbol{x}\int d\boldsymbol{v}[G(\boldsymbol{x})-mv^2/2]^{-1/2}}. \tag{2.27}$$

Using

$$mv^2/2 \equiv sG(\boldsymbol{x}), \quad mv\,dv = ds G(\boldsymbol{x}), \tag{2.28}$$

TABLE II. ''Longitudinal breathing'' oscillations.

c/a	$\left(\frac{u_{\max}}{w_{\max}}\right)_{\text{analytic}}$	$\left(\frac{u_{\max}}{w_{\max}}\right)_{\text{numerical}}$
2	-0.10	-0.10 ± 0.03
3	-0.07	-0.05 ± 0.01
4	-0.05	-0.03 ± 0.01
5	-0.04	-0.03 ± 0.01

we have

$$\langle mv^2\rangle = \frac{2\int d\boldsymbol{x}G^2(\boldsymbol{x})\int_0^1 ds s^{3/2}(1-s)^{-1/2}}{\int d\boldsymbol{x}G(\boldsymbol{x})\int_0^1 ds s^{1/2}(1-s)^{-1/2}}, \tag{2.29}$$

or

$$\langle m\dot{x}^2\rangle = \langle m\dot{z}^2\rangle = \frac{k_s}{2\kappa^2}\frac{g_2}{g_1}, \tag{2.30}$$

where

$$g_n \equiv \frac{1}{a^3}\int d\boldsymbol{x} g^n(\boldsymbol{x}), \tag{2.31}$$

with $g(\boldsymbol{x})$ defined by Eq. (2.13). We use a, the transverse beam radius at $z=0$, as the unit of length.

C. Dimensionless parametrization

The definition of the dimensionless function $g(\boldsymbol{x})$ in Eq. (2.14) and the fitting to the ellipsoid of Eq. (2.15) implies that the dimensionless parameters g_1 and g_2 are functions only of κa and c/a. Since the charge density in Eq. (2.7) can be written as

$$\rho(\boldsymbol{x}) = (Q/a^3)[g(\boldsymbol{x})/g_1], \tag{2.32}$$

a Poisson-type code can be used to obtain the potential and fields from the distribution of charge. From a dimensionless perspective, this leads to

$$\langle xE_x\rangle = (Q/a\epsilon_0)\phi_x, \quad \langle zE_z\rangle = (Q/a\epsilon_0)\phi_z, \tag{2.33}$$

where ϕ_x and ϕ_z are functions only of κa and c/a, determined numerically. Using Eqs. (2.11) and (2.13), we find that

$$e\langle xE_x\rangle = k_s g_1 \phi_x a^2, \quad e\langle zE_z\rangle = k_s g_1 \phi_z a^2. \tag{2.34}$$

From Eq. (2.26), we obtain for the rms tune depressions

$$\frac{1-\eta_x^2}{\eta_x^2} = \frac{2\kappa^2 a^2 g_1^2 \phi_x}{g_2}, \quad \frac{1-\eta_z^2}{\eta_z^2} = \frac{2\kappa^2 a^2 g_1^2 \phi_z}{g_2}, \tag{2.35}$$

noting that η_x^2 and η_z^2 are also functions only of κa and c/a. Equation (2.24) also makes it clear that k_x/k_z is also a function only of κa and c/a.

Finally, we put Eq. (2.11) into the dimensionless form

$$Q/e = (\epsilon_0/e^2)k_s a^3 g_1. \tag{2.36}$$

Using Eq. (2.3), we can write Eq. (2.23) as

$$\epsilon_x^2 = \frac{k_s a^2}{mc_0^2}\frac{g_2}{g_1}\frac{\langle x^2\rangle}{2\kappa^2 a^2}, \quad \epsilon_z^2 = \frac{k_s a^2}{2mc_0^2}\frac{g_2}{g_1}\frac{\langle z^2\rangle}{2\kappa^2 a^2}, \tag{2.37}$$

so that the number of ions in a bunch can be written as

$$\frac{Q}{e} = \frac{2\kappa^2 a^2 g_1^2}{g_2}\frac{a^2}{\langle x^2\rangle}\frac{\epsilon_x^2}{4\pi r_p a} = \frac{2\kappa^2 a^2 g_1^2}{g_2}\frac{a^2}{\langle z^2\rangle}\frac{\epsilon_z^2}{4\pi r_p a}, \tag{2.38}$$

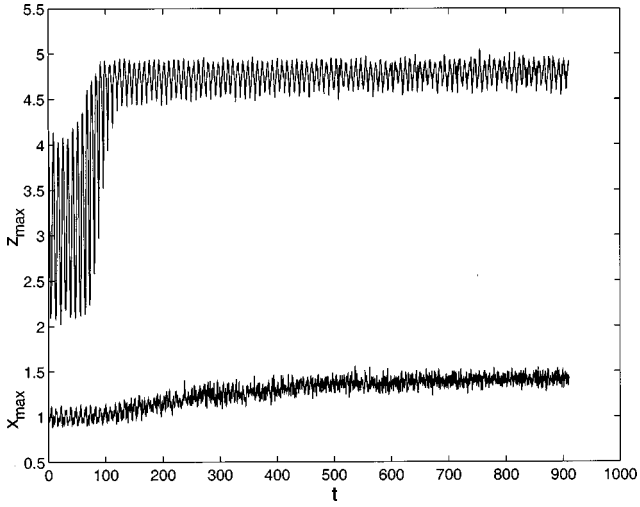

FIG. 6. Maximum x and z as a function of time in arbitrary units. In this figure one longitudinal breathing oscillation takes about 8.3 such units. ($c/a=3$, $\eta_x=0.65$, $\eta_z=0.49$, $\mu_z=1.4$, $\mu_x=0.94$).

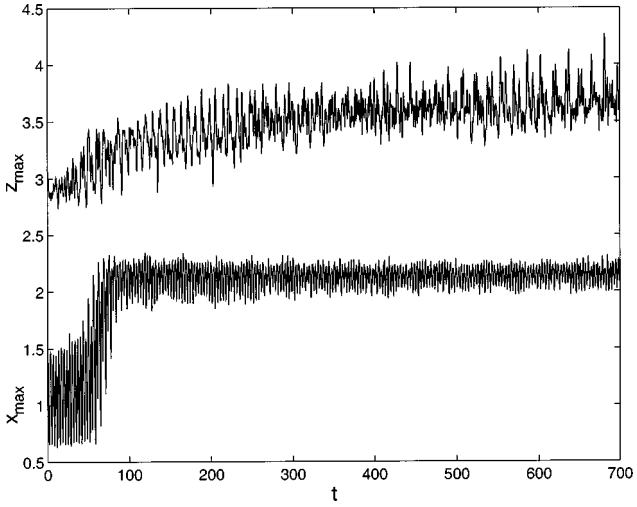

FIG. 8. Maximum x and z as a function of time in arbitrary units for a primarily transverse mode ($c/a=3$, $\eta_x=0.65$, $\eta_z=0.49$, $\mu_x=1.5$, $\mu_z=1.027$).

where

$$r_p \equiv e^2/(4\pi\epsilon_0 m c_0^2) \tag{2.39}$$

is the classical radius of the proton. Since $\langle x^2\rangle/a^2$ is also a dimensionless parameter depending only on κa and c/a, we write

$$Q/e = q(\kappa a, c/a)(\epsilon_x^2/4\pi r_p a), \tag{2.40}$$

where

$$q(\kappa a, c/a) = \frac{2\kappa^2 a^2 g_1^2}{g_2}\frac{a^2}{\langle x^2\rangle} = \frac{1-\eta_x^2}{\eta_x^2}\frac{a^2}{\phi_x\langle x^2\rangle} \tag{2.41}$$

is a dimensionless parameter proportional to the bunch charge.

To summarize, we choose the shape of the spheroidal bunch (c/a) and increase κa until the tune depressions η_x and/or η_z become excessive. This determines the required force gradients, and specifies the number of ions that are contained within the bunch as a multiple of the dimensionless quantity $\epsilon_x^2/4\pi r_p a$. What remains is to explore the κa, c/a space numerically for the current carrying capacity and for the likelihood, extent, and rate of halo production.

III. NUMERICAL INVESTIGATION OF PARAMETERS

A. Bunch parameters

We obtain the desired values of α_ℓ in Eq. (2.14) for different c/a and values of κa in the range of interest [12], by minimizing $\oint ds g^2(\boldsymbol{x})$ along the elliptical boundary of Eq. (2.15). We show a contour plot of $g(\boldsymbol{x})$ in Fig. 2 for the typical case $c/a=3$, $\kappa a=3.0$. This range of parameters corresponds to the proposed bunches for the Accelerator Production of Tritium (APT) project [12]. In Fig. 3 we plot $(1-\eta_x^2)/\eta_x^2$ vs $\kappa^2 a^2$ for each value of c/a and find the universal fit

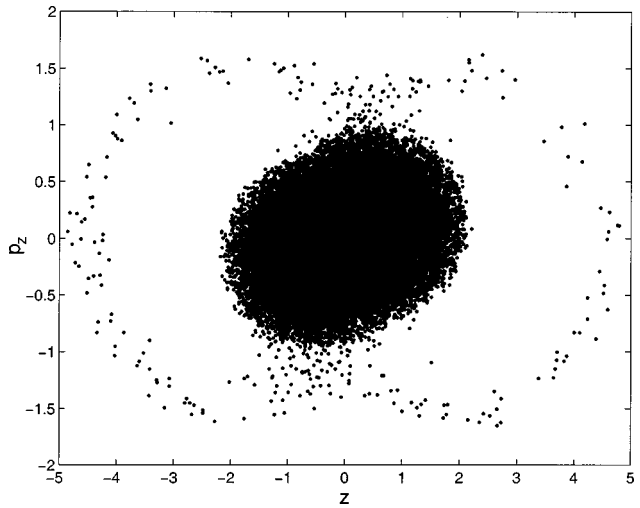

FIG. 7. Phase space diagram of a longitudinal halo ($c/a=3$, $\eta_x=0.65$, $\eta_z=0.49$, $\mu_z=1.4$, $\mu_x=0.94$).

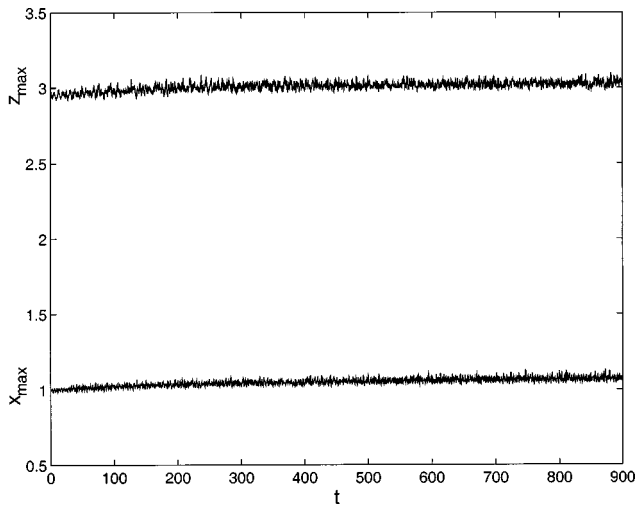

FIG. 9. Maximum x and z as a function of time for initially matched beam $\mu=1.0$ ($c/a=3$, $\eta_x=0.33$, $\eta_z=0.25$).

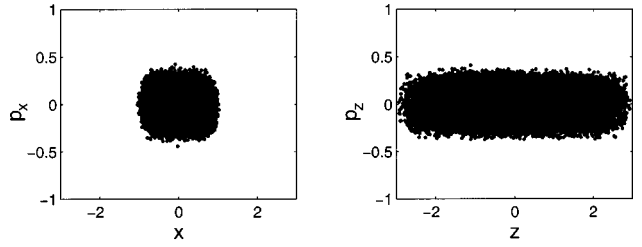

FIG. 10. Phase space diagrams at $t=900$ of initially matched beam $\mu=1.0$ for severe tune depressions ($c/a=3$, $\eta_x=0.33$, $\eta_z=0.25$).

$$\frac{1-\eta_x^2}{\eta_x^2}=\left(\frac{\kappa a}{2.82}\right)^2\left(\frac{c}{a}\right)^{0.20},$$

$$\eta_x=[1+(\kappa a/2.82)^2(c/a)^{0.20}]^{-1/2}, \tag{3.1}$$

where η_x is accurate to a few percent for the range of κa of interest in halo formation.

Similarly, we find a linear dependence of $(1-\eta_z^2)/\eta_z^2$ on $\kappa^2 a^2$ and construct the universal fit:

$$\frac{1-\eta_z^2}{\eta_z^2}=\left(\frac{\kappa a}{2.82}\right)^2\left(\frac{c}{a}\right)^{0.91},$$

$$\eta_z=[1+(\kappa a/2.82)^2](c/a)^{0.91}]^{-1/2}, \tag{3.2}$$

where η_z is again accurate to a few percent for the range of κa of interest.

Finally we compute $q(\kappa a,c/a)$ using Eq. (2.41) and again find the universal fit

$$q(\kappa a,c/a)\cong 44\kappa^2 ac. \tag{3.3}$$

In Figs. 4 and 5, we plot η_x versus q and η_z versus q for different c/a, respectively.

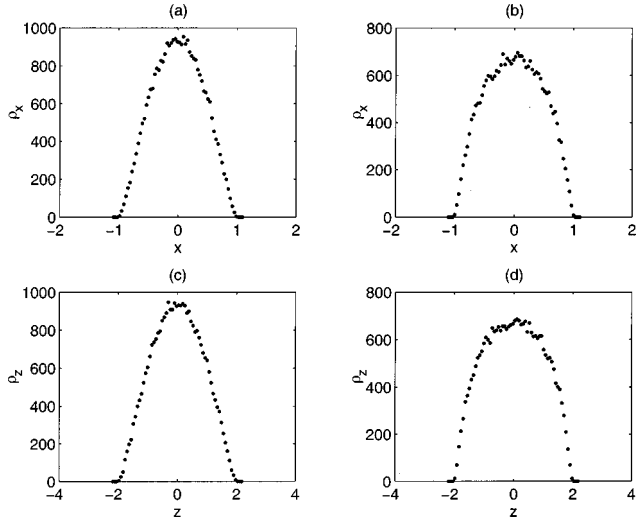

FIG. 11. Density profiles for the modest and severe tune depressions for $c/a=2$. (a) ρ_x vs x ($\eta_x=0.94$). (b) ρ_x vs x ($\eta_x=0.29$). (c) ρ_z vs z ($\eta_z=0.90$). (d) ρ_z vs z ($\eta_z=0.22$).

B. Implications

The surprising simplicity of Eqs. (3.1)–(3.3) makes it easy to explore the parameter space. It is clear from Eqs. (3.1) and (3.2) that, for $c/a>1$, η_z will always be less than η_x. Thus we can expect that the longitudinal tune depression will be more severe than the transverse tune depression and that a longitudinal halo is more likely to form first. This turns out to be the case, as we shall see in the actual simulations. Furthermore, if halo formation (for a given mismatch) is controlled by the extent of the longitudinal tune depression, according to Fig. 5, we can accelerate slightly larger currents for higher c/a if the longitudinal halo is of primary concern. Similarly, Fig. 4 shows that we can accelerate significantly more current for higher c/a if the transverse halo is of primary concern, which may be the case for a primarily transverse mismatch.

IV. NORMAL MODES

A. Analytic model

If we confine our attention to axisymmetric beam bunches, it is clear that there are two independent breathing-like mismatch parameters, associated with the transverse and longitudinal deviations in shape from the matched beam determined by Eqs. (2.14) and (2.15). Unfortunately an analytic treatment of the mismatch oscillations is not available for our distribution. We will therefore assume, for this purpose only, that the spheroidal bunch has uniform charge density, and comes from a self-consistent treatment for which the envelope equations are

$$m\frac{d^2a}{dt^2}+k_x a=Ka\sigma_x+\frac{\epsilon_x^2}{a^3}, \tag{4.1}$$

$$m\frac{d^2c}{dt^2}+k_z c=Kc\sigma_z+\frac{\epsilon_z^2}{c^3}, \tag{4.2}$$

where $K=3eQ/8\pi\epsilon_0$. Here

$$\sigma_x=\int_0^\infty \frac{ds}{(a^2+s)^2(c^2+s)^{1/2}}\equiv\lambda_{10}, \tag{4.3}$$

$$\sigma_z=\int_0^\infty \frac{ds}{(a^2+s)(c^2+s)^{3/2}}\equiv\lambda_{01}, \tag{4.4}$$

where

$$\lambda_{pq}=\int_0^\infty \frac{ds}{(a^2+s)^{p+1}(c^2+s)^{q+1/2}}. \tag{4.5}$$

We now expand around the equilibrium distribution by replacing a and c by $a+u$ and $c+w$. In the linear approximation, for u and w, this leads to the coupled equations

$$m\frac{d^2u}{dt^2}+k_x u=Ku\sigma_x-\frac{3\epsilon_x^2 u}{a^4}+Kau\frac{\partial\sigma_x}{\partial a}+Kaw\frac{\partial\sigma_x}{\partial c} \tag{4.6}$$

and

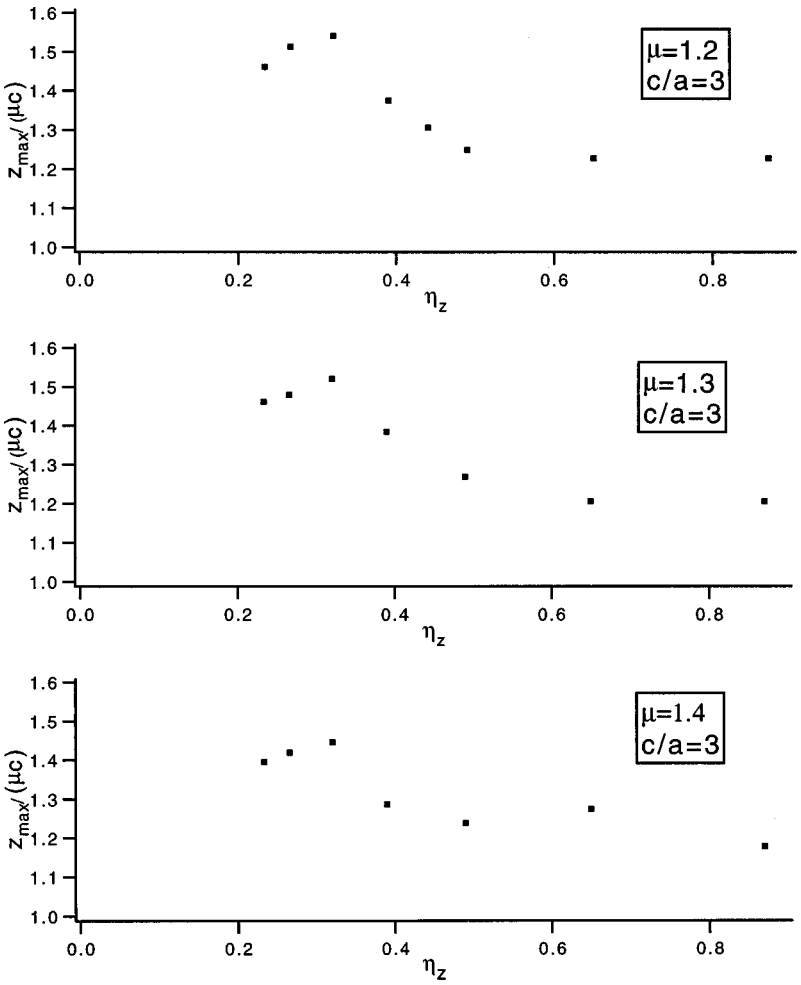

FIG. 12. Longitudinal halo extent for different mismatches.

$$m\frac{d^2w}{dt^2}+k_z w=Kw\sigma_z-\frac{3\epsilon_z^2 w}{c^4}+Kcw\frac{\partial\sigma_z}{\partial c}+Kcu\frac{\partial\sigma_z}{\partial a}. \tag{4.7}$$

The derivatives in the coefficients can be written as

$$\frac{\partial\sigma_x}{\partial a}=-4a\lambda_{20},\quad \frac{\partial\sigma_x}{\partial c}=-c\lambda_{11}, \tag{4.8}$$

$$\frac{\partial\sigma_z}{\partial a}=-2a\lambda_{11},\quad \frac{\partial\sigma_z}{\partial c}=-3c\lambda_{02}. \tag{4.9}$$

In addition we express all terms in Eqs. (4.1) and (4.2) in terms of the tune depressions η_x and η_z. Specifically, we write

$$k_x=\frac{K\sigma_x}{1-\eta_x^2}=\frac{K\lambda_{10}}{1-\eta_x^2},\quad k_z=\frac{K\lambda_{01}}{1-\eta_z^2} \tag{4.10}$$

and

$$\frac{\epsilon_x^2}{a^4}=\frac{\eta_x^2}{1-\eta_x^2}K\lambda_{10},\quad \frac{\epsilon_z^2}{c^4}=\frac{\eta_z^2}{1-\eta_z^2}K\lambda_{01}. \tag{4.11}$$

This permits us to rewrite Eqs. (4.6) and (4.7) as

$$\ddot{u}+\nu_x^2 u=-\nu_{xz}^2 w, \tag{4.12}$$

$$\ddot{w}+\nu_z^2 w=-2\nu_{xz}^2 u, \tag{4.13}$$

where

$$\nu_x^2=\frac{K}{m}\left[\frac{4\eta_x^2}{1-\eta_x^2}\lambda_{10}+4a^2\lambda_{20}\right], \tag{4.14}$$

$$\nu_z^2=\frac{K}{m}\left[\frac{4\eta_z^2}{1-\eta_z^2}\lambda_{01}+3c^2\lambda_{02}\right], \tag{4.15}$$

$$\nu_{xz}^2=\frac{K}{m}ac\lambda_{11}. \tag{4.16}$$

For a long narrow bunch ($c\gg a$), one finds that

$$\lambda_{10}\cong\frac{1}{a^2c},\quad \lambda_{20}\cong\frac{1}{2a^4c},\quad \lambda_{11}\cong\frac{1}{a^2c^3} \tag{4.17}$$

and

$$\lambda_{01}\cong\frac{2}{c^3}\left(\ln\frac{2c}{a}-1\right),\quad \lambda_{02}\cong\frac{2}{c^5}\left(\ln\frac{2c}{a}-\frac{4}{3}\right), \tag{4.18}$$

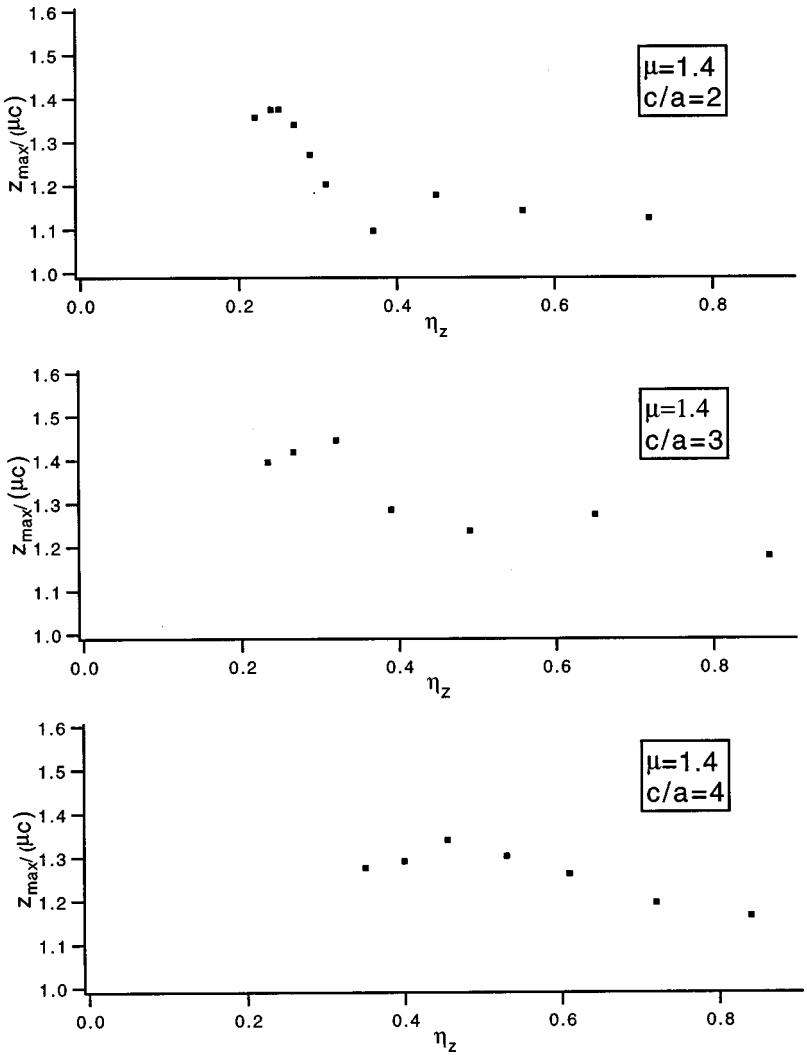

FIG. 13. Longitudinal halo extent for different c/a.

so that

$$\nu_x^2 \cong \frac{3eQ}{4\pi\epsilon_0 ma^2 c}\left(\frac{1+\eta_x^2}{1-\eta_x^2}\right), \tag{4.19}$$

$$\nu_z^2 \cong \frac{3eQ}{4\pi\epsilon_0 mc^3}\left[\left(\frac{3+\eta_z^2}{1-\eta_z^2}\right)\not{\ell} n\frac{2c}{a} - \frac{4}{1-\eta_z^2}\right], \tag{4.20}$$

$$\nu_{xz}^2 \cong \frac{3eQ}{8\pi\epsilon_0 mac^2}. \tag{4.21}$$

The solution to Eqs. (4.12) and (4.13) consists of two coupled modes. With $c \gg a$, it is clear that the high-frequency mode ($\nu_h \cong \nu_x$) is primarily transverse with u and w in phase and

$$\frac{w_{\max}}{u_{\max}} \cong \frac{2\nu_{xz}^2}{\nu_x^2} \cong \frac{a}{c}\frac{1-\eta_x^2}{1+\eta_x^2} \text{ (high-frequency mode)} \tag{4.22}$$

while the low-frequency mode ($\nu_{\not{\ell}} \cong \nu_z$) is primarily longitudinal with u and w 180° out of phase and

$$\frac{u_{\max}}{w_{\max}} \cong -\frac{\nu_{xz}^2}{\nu_x^2} \cong -\frac{a}{2c}\frac{1-\eta_x^2}{1+\eta_x^2}. \tag{4.23}$$

The high-frequency mode strongly resembles the mode that dominated the 2D analyses and simulations. The low-frequency mode is new, but leads to very similar behavior in the longitudinal phase space, namely, a stable region bounded by an inner separatrix, and an outer separatrix that forms the locus of a longitudinal halo if it develops.

The above analysis for small mismatch oscillations is not valid for the 3D bunch of Sec. II in which the charge density is not uniform in the ellipsoid. Nevertheless, the final form of Eqs. (4.12) and (4.13) is likely to apply, with somewhat modified forms for the parameters from those given in Eqs. (4.19)–(4.21). And the results in Eqs. (4.22) and (4.23) should give the correct order of magnitude of the effect of ''coupling'' for long narrow bunches.

B. Numerical implementation

As an illustrative example, we take the bunch charge appropriate to $\kappa a = 3.0$, which corresponds to $\eta_z = 0.56$, 0.49, 0.46, 0.43, $\eta_x = 0.66$, 0.65, 0.64, 0.64 for $c/a = 2,3,4,5$, respectively. Using these values for a stationary distribution in

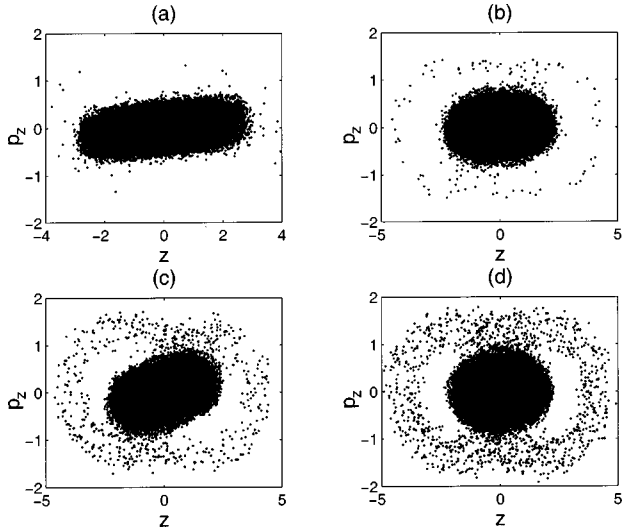

FIG. 14. Dependence of halo intensity on the mismatch for $c/a=3$, $\eta_x=0.65$, $\eta_z=0.49$ (with 32 768 particles plotted). (a) $\mu=1.1$. (b) $\mu=1.2$. (c) $\mu=1.3$. (d) $\mu=1.4$.

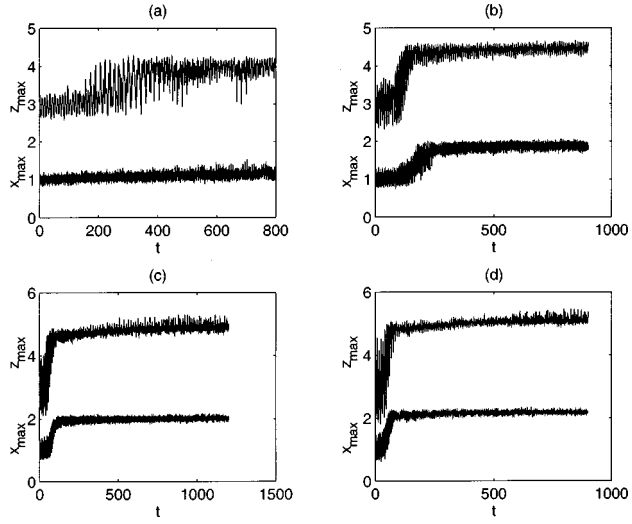

FIG. 16. Halo development for comparable mismatches ($c/a=3$, $\eta_x=0.65$, $\eta_z=0.49$). (a) $\mu=1.1$. (b) $\mu=1.2$. (c) $\mu=1.3$. (d) $\mu=1.4$.

Eqs. (4.22) and (4.23) that was derived for a uniformly charged spheroidal beam, we obtain the analytic predictions for the relative longitudinal and transverse amplitudes of the normal modes. By exploring the numerical oscillations obtained in simulations with slightly mismatched stationary distribution, we obtain the corresponding numerical values. Results are then presented in Table I for the ''transverse breathing'' oscillations, and in Table II for the ''longitudinal breathing'' oscillations. We see that the predictions of the analytic model of a uniformly charged spheroidal beam for the amplitudes of the normal modes are in reasonable agreement with simulation results for our self-consistent stationary distribution.

We have developed a 3D particle-in-cell (PIC) code to test the analytic model described above, and to explore halo formation. The single-particle equations of motion are integrated using a symplectic, split-operator technique [13]. The space charge calculation uses area weighting (''cloud in cell'') and implements open boundary conditions with the Hockney convolution algorithm [14]. The code runs on parallel computers, and, in particular, the space charge calculation has been optimized for parallel platforms using the Ferrell-Bertschinger method [15].

We initially populate the 6D phase space according to Eq. (2.1), and then mismatch the x,y,z coordinates by factors $\mu_x=\mu_y=1+\delta a/a$, $\mu_z=1+\delta c/c$ and the corresponding momenta by $1/\mu_x=1/\mu_y$, $1/\mu_z$. In Fig. 6, we start with $\delta c/c=0.4$, $\delta a/a=0.06$ (the primarily longitudinal mode for $c/a=3$, $\kappa a=3$), plotting the maximum x and z among the million particles in our run as a function of time (in the Lorentz frame of the bunch). The development of a longitudinal halo is clearly visible. In Fig. 7, the longitudinal phase space (in phase space diagrams we plot only 32 768 particles from one million particles used in simulations) clearly shows

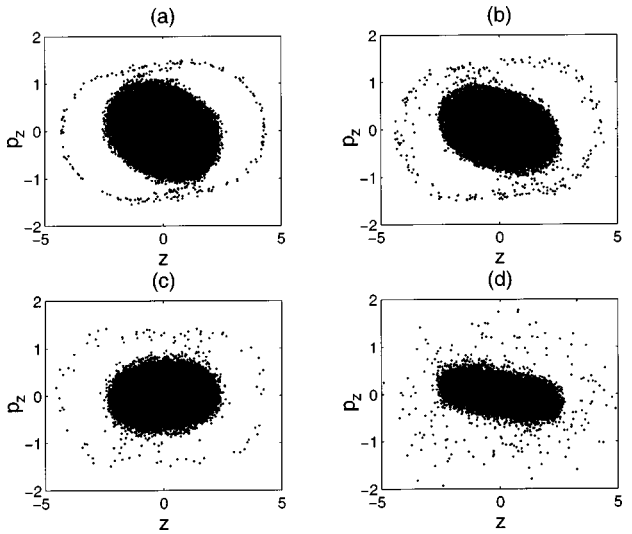

FIG. 15. Dependence of halo intensity on tune depression for $c/a=3$, $\mu=1.2$. (a) $\eta_z=0.87$. (b) $\eta_z=0.65$. (c) $\eta_z=0.49$. (d) $\eta_z=0.32$.

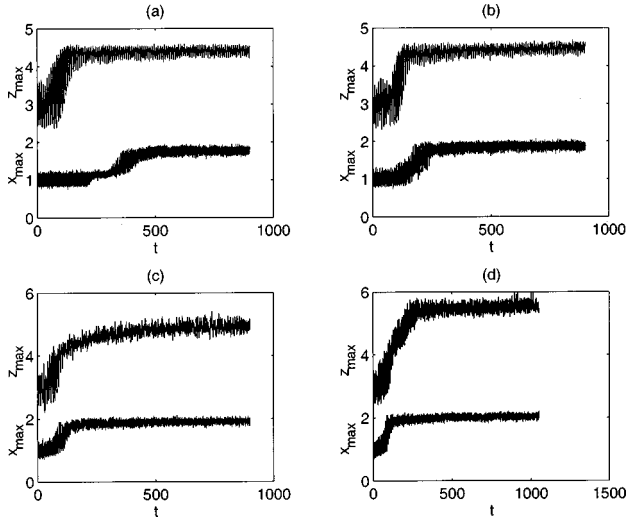

FIG. 17. Dependence of the rate of halo development on tune depressions for $c/a=3$, $\mu=1.2$. (a) $\eta_x=0.79$, $\eta_z=0.65$. (b) $\eta_x=0.65$, $\eta_z=0.49$. (c) $\eta_x=0.53$, $\eta_z=0.39$. (d) $\eta_x=0.45$, $\eta_z=0.32$.

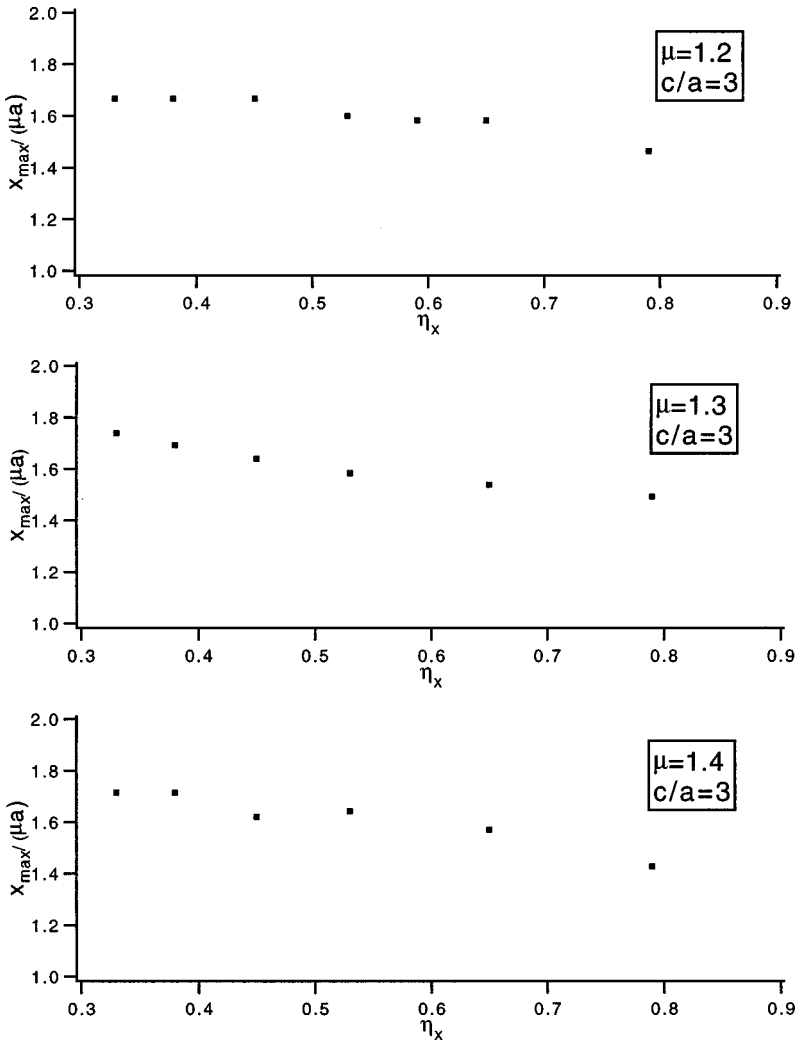

FIG. 18. Transverse halo extent for different mismatches.

the typical peanut diagram for a halo. Similar results are obtained for different tune depressions and for other mismatches. If we repeat the calculation for $\delta a/a=0.5$, $\delta c/c=0.027$, for example (the primarily transverse mode for $c/a=3$, $\kappa a=3$), a transverse halo develops first as can be seen in Fig. 8.

V. ORBIT SIMULATIONS

A. Stability of the matched distribution

The analytic theory for the 2D matched KV beam suggests that the beam becomes unstable for severe tune depression. Both numerical studies of the unstable modes and multiparticle simulations for the 2D breathing KV beam with zero mismatch confirmed that the beam is unstable for tune depressions below $\eta=0.4$ [5]. However, no halo was observed in the corresponding 2D simulations.

Similar studies for other rms matched distributions that are not stationary solutions of the Vlasov equation showed the existence of a halo for a severe tune depression and zero mismatch parameter [9]. The existence of a halo for such rms matched distributions was attributed to the unavoidable plasma oscillations generated by the initial density-redistribution process, which is clearly shown in [9].

In our current 3D calculations no such redistribution occurs since we start with a self-consistent stationary distribution. In fact, an initially matched beam seems to be very stable even for severe tune depressions. In Fig. 9 we plot the maximum x and z among the million particles in our run as a function of time for an initially matched beam, and in Fig. 10 we show the phase space diagram for $c/a=3$, $\eta_x=0.33$, $\eta_z=0.25$. The fact that our nonlinear (nonlinear space charge forces) stationary 6D phase space distribution is stable for severe tune depressions, unlike the linear KV distribution, is not surprising since the real nonlinear distributions in the actual accelerator are expected to be more stable than the singular linear KV beam. For completeness, in Fig. 11 we show the transverse and longitudinal density distribution profiles for the modest and severe tune depressions.

B. Longitudinal halo

1. Halo extent

Due to the fact that longitudinal tune depression is always less than the transverse one for elongated bunches the longitudinal halo is our primary focus. An important quantity is the ratio of the halo radius to that of the matched distribution. We performed a systematic study for different c/a and

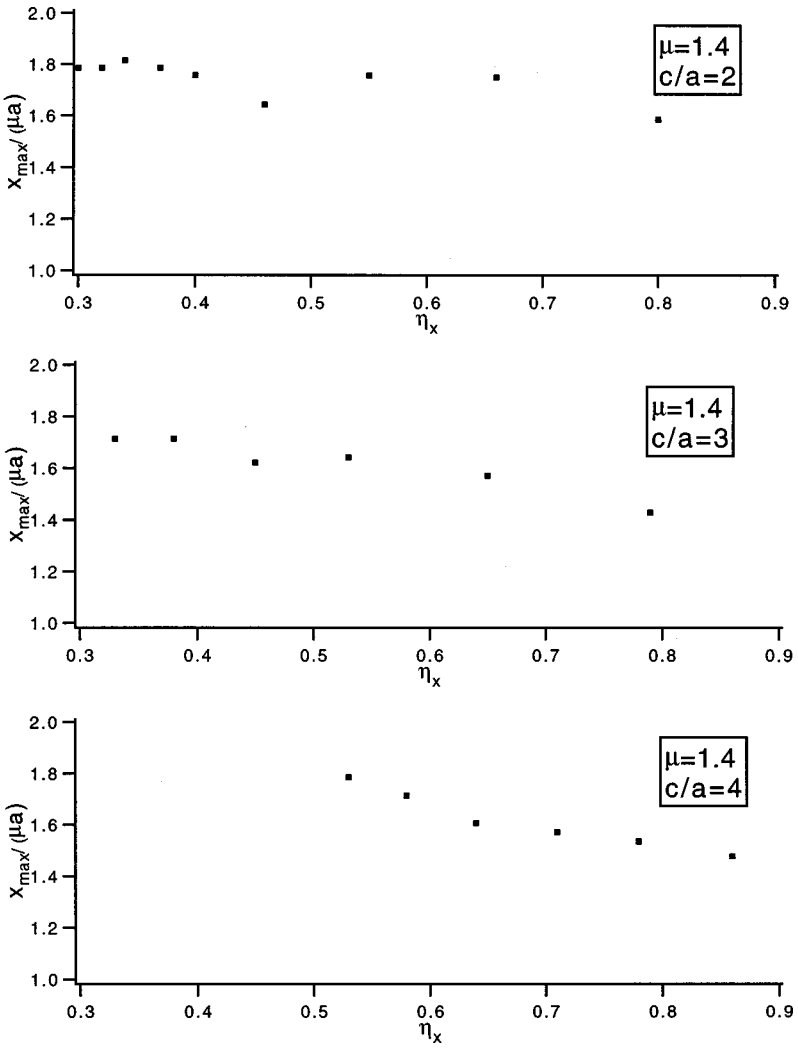

FIG. 19. Transverse halo extent for different c/a.

mismatch factors in the range of interest [12], by looking at the halo extent at the time when the beam comes to a roughly saturated state after the development of a halo. Our new result is the dependence of the halo extent on tune depression shown in Figs. 12 and 13 for $c/a=2,3,4$ and mismatch parameters $\mu=1.2,1.3,1.4$ being the same in all directions x,y,z (for later reference note that μ without a subscript automatically means similar mismatch in all directions). One sees a significant increase in halo extent for severe tune depressions. In addition, the halo extent clearly depends on the mismatch parameter. The approximately linear dependence of the halo extent on the mismatch factor μ indicates that a serious effort should be made to match the beam to the channel as accurately as possible.

2. Halo intensity

Simulation results show that the halo intensity (roughly defined as the fraction of particles outside the core in phase space) depends primarily on the mismatch. Figure 14 presents the phase space diagram (with only 32 768 particles plotted) after the halos have stabilized, for $\eta_x=0.65, \eta_z=0.49$ $(c/a=3)$ with several mismatches $\mu=1.1,1.2,1.3,1.4$.

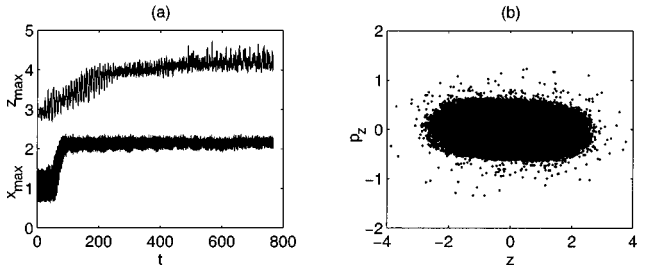

FIG. 20. $c/a=3$, $\mu_x=\mu_y=1.5$, $\mu_z=1.05$. (a) Maximum x and z as a function of time. (b) z,p_z phase space diagram.

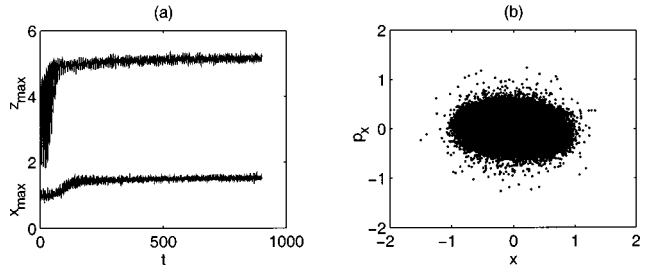

FIG. 21. $c/a=3$, $\mu_z=1.5$, $\mu_x=\mu_y=1.05$. (a) Maximum x and z as a function of time. (b) x,p_x phase space diagram.

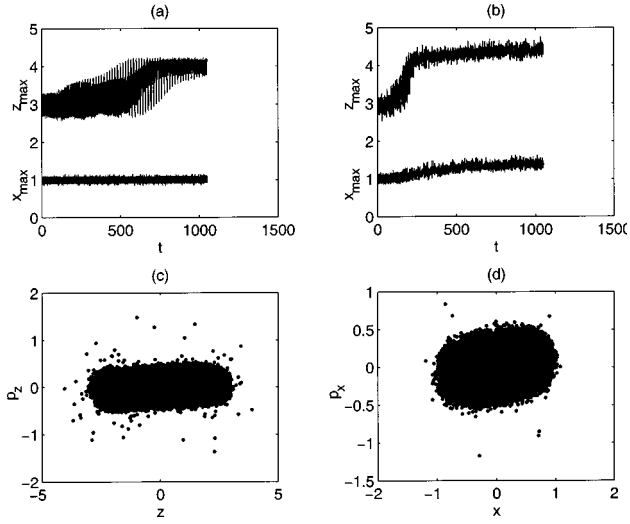

FIG. 22. $c/a=3$, $\mu=1.1$. (a) Maximum x and z ($\eta_x=0.93$, $\eta_z=0.87$). (b) Maximum x and z ($\eta_x=0.53$, $\eta_z=0.39$). (c) z,p_z phase space diagram, $\eta_x=0.53$, $\eta_z=0.39$. (d) x,p_x phase space diagram, $\eta_x=0.53$, $\eta_z=0.39$.

Severe mismatches lead to several percent of the particles in the halo, which is clearly outside acceptable limits. In Fig. 15 we present the phase space diagram for different tune depressions $\eta_z=0.87,0.65,0.49,0.32$ with $\mu=1.2$ ($c/a=3$) for which the fraction of particles in the halo is about 0.5%.

No significant dependence of halo intensity on the tune depression is seen.

However, for tune depression $\eta_z\leqslant 0.4$ the clear peanut diagram in the longitudinal phase space now has a chaotic behavior.

3. Rate of halo development

One more important feature is how fast the halo develops. We first make the observation that for comparable mismatches the longitudinal halo develops much faster than the transverse halo when the mismatches and/or tune depressions are not severe. Such behavior simply occurs because for fixed charge we have $\eta_z<\eta_x$ for elongated bunches. For severe mismatches and/or tune depressions both the longitudinal and transverse halos develop very quickly. A typical picture is shown in Fig. 16.

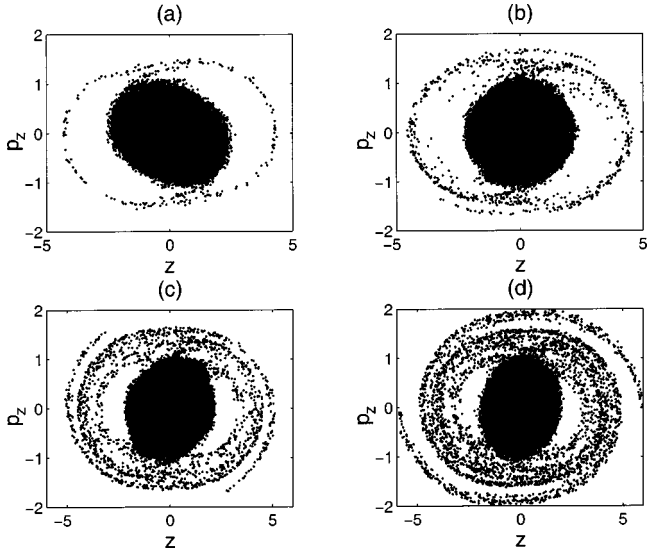

FIG. 23. Filamentation process at $t=900$, $c/a=3$, $\eta_x=0.93$, $\eta_z=0.87$. (a) $\mu=1.2$. (b) $\mu=1.3$. (c) $\mu=1.4$. (d) $\mu=1.6$.

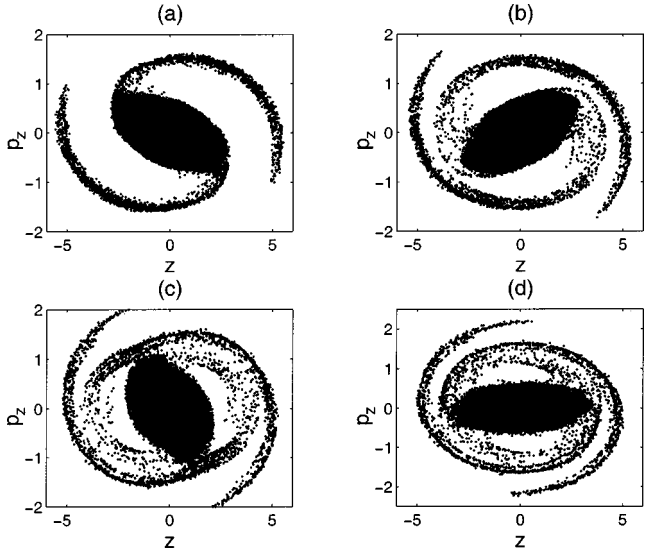

FIG. 24. Evaluation of filamentation for $c/a=3$, $\eta_z=0.87$, $\mu=1.6$. (a) $t=250$. (b) $t=350$. (c) $t=450$. (d) $t=550$.

Of particular interest is the clear dependence on tune depression. Specifically, for more severe tune depression the halo starts to develop earlier as can be seen in Fig. 17 where the development of the halo is shown for $c/a=3$, $\mu=1.2$ and different tune depressions.

4. Pure longitudinal mismatch

Another important characteristic of the longitudinal halo is its dependence on the mismatch when there is no mismatch in the radial direction. The number of particles in the halo drops dramatically with μ_z. In fact, we see no halo for $\mu_z<1.2$ ($<20\%$ longitudinal mismatch). Note that the situation changes when the effect of coupling is significant, as discussed in a later section.

C. Transverse halo

We now perform a systematic study of the halo extent for a transverse halo. As can be seen in Figs. 18 and 19 for $c/a=2,3,4$ and $\mu=1.2,1.3,1.4$ with similar mismatches in x,y,z, the halo extent increases slightly with increasing space charge. In fact, the increase is similar to the one seen

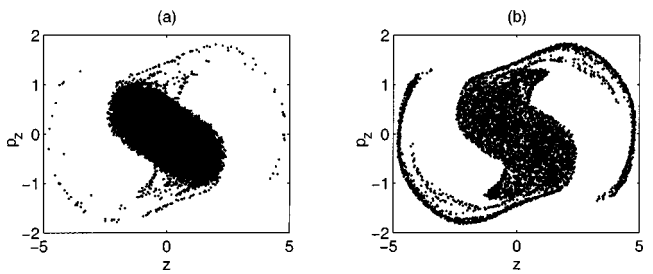

FIG. 25. Halo structure at $t=80$ for $c/a=3$, $\eta_x=0.65$, $\eta_z=0.49$, $\mu=1.4$. (a) without low density cut (b) with low density cut.

for nonlinear stationary distributions in 2D simulations [7] and nonstationary rms matched distributions [9]. However, the dependence on tune depression does not disappear with increasing mismatch as was seen in [9], where no dependence on the tune depression for $\mu \geqslant 1.3$ was observed. In addition, the halo extent simply scales with the mismatch parameter. As was the case for the longitudinal halo, we find that the halo intensity is governed primarily by the mismatch.

We already noted that the transverse halo develops significantly more slowly than the longitudinal halo for comparable mismatches. The halo usually saturates after a few hundred breathing periods. We also note that, for a pure transverse mismatch ($\mu_z = 1.0$), the transverse halo is observed even for $\mu_x = \mu_y = 1.15$.

In general the transverse halo closely duplicates all the features observed for nonlinear stationary distributions in 2D simulations [7]. The agreement between 2D and 3D simulations is very good. The only two significant differences seen are related to the rate of halo development. In the present 3D simulations there is a clear dependence on the tune depression (see Fig. 17), which was not the case in the corresponding 2D simulations [7]. The second difference is that the transverse halo in the 3D simulations develops significantly faster than in 2D for comparable mismatches and tune depressions.

D. Coupling effects

Most of the previous studies were concerned with halos in long or continuous beams. In the current work we address the question of halo formation in a beam bunch, where we clearly now have coupling between the longitudinal and transverse motion. Due to the coupling between r and z, a transverse or longitudinal halo is observed even for a very small mismatch (less than 10%) as long as there is a significant mismatch in the other plane. As an example, Fig. 20 shows a clear longitudinal halo for $\mu_z = 1.05$, $\mu_x = \mu_y = 1.5$ (5% longitudinal mismatch), and Fig. 21 shows a clear transverse halo for $\mu_x = \mu_y = 1.05$, $\mu_z = 1.5$ (5% transverse mismatch).

The effect of coupling is visible even for modest mismatches. For example, a 20% longitudinal mismatch is required to develop a longitudinal halo when the transverse mismatch is zero. However, when there is a mismatch in all directions we see a halo even when $\mu_z = \mu_x = \mu_y = 1.1$ (10% mismatch in all directions) as shown in Fig. 22. Such behavior clearly shows the importance of the coupling effect.

E. Halo structure

In the limit of low space charge the longitudinal phase space diagram closely resembles the filamentation process described by Jameson [10]. This results in the phase space ellipse becoming distorted into a spiral-like structure depending on the mismatch factor, as can be seen in Fig. 23 for $c/a = 3$, $\eta_z = 0.87$, $\eta_x = 0.93$. As the particles are expelled from the core they lead to a filamented core or produce new tails. The new tails are continuously pushed out from the core, but always stay inside the original tail as shown in Fig. 24.

This phenomenon provides a rough description of the formation of a halo. When a significant portion of the particles is expelled from the origin the particles inside the core see a reduced charge, which results in a new set of expelled particles that follow separatrices in the phase space that are closer to the core. For higher space charge the beam undergoes more severe density redistribution and the detailed halo structure becomes more diffuse. The result is a peanut-shaped diagram in longitudinal phase space without an obvious filamentation structure (Figs. 14 and 15). The reason that we do not observe the filamentation in this case is that most of the plotted particles are in the core. To get better resolution of the halo region we perform a low density phase space cut. In this procedure, we choose a threshold phase space density just above that in the halo and plot all halo particles. In the high density region we plot only the fraction of the particles corresponding to the threshold density. The result is seen in Fig. 25, where we show the longitudinal phase space diagram with and without the low density cut for $c/a = 3$, $\mu = 1.4$, $\eta_x = 0.65$, $\eta_z = 0.49$. In this way one sees how the spiral structure develops into the more familiar peanut diagram.

This peanut diagram in the longitudinal phase space is very clear for relatively long bunches ($c/a \geqslant 3$). For short bunches the diagram is distorted by the appearance of particles between the core and the halo in the limit of low space charge. This effect is probably related to the stronger coupling between the transverse and longitudinal motion for short bunches, and its effect on the filamentation process.

VI. SUMMARY

Most of the previous studies were concerned with halos in long beams. In the current work we address the question of halo formation in a beam bunch that is of particular interest for the Accelerator Production of Tritium project, where relatively short bunches are proposed [12].

We have constructed, analytically and numerically, a new class of 6D phase space stationary distributions for an azimuthally symmetric beam bunch of arbitrary charge in the shape of a prolate spheroid (see Fig. 2), and have determined the rms tune depressions η_x, η_z as a function of the bunch charge and eccentricity (see Figs. 4 and 5). The stationary distribution allows us to study the halo development mechanism in 3D beam bunches where no phase space redistribution takes place. Our choice of parameters automatically assures equipartition. In our calculations the beam remains equipartitioned through the channel. We therefore study the halo development in 3D beams that are in thermal equilibrium, without the redistribution introduced by any equipartition process that may take place. Such an approach gives us an excellent chance to investigate the major mechanism of halo formation associated purely with the beam mismatch.

We then use a PIC code with smoothed linear external focusing forces, in which the initial stationary distribution is mismatched in both the transverse and longitudinal directions, and find that both transverse and longitudinal halos can develop, depending on the choice of tune depressions and mismatches. A new result, due to the coupling between the r and z planes, is that a transverse or longitudinal halo is ob-

served for a mismatch less than 10% if the mismatch in the other plane is large.

Our main conclusion is that the longitudinal halo is of great importance because it develops earlier than the transverse halo for elongated bunches with comparable longitudinal and transverse mismatches, and because it occurs even for mismatches of order 10%. In addition, the control of the longitudinal halo could be challenging if the phase width of a beam bunch in the RF bucket cannot be made sufficiently small. The main characteristics of the longitudinal and transverse halo are discussed in Sec. V.

Now that we have established the parameters that lead to halo formation in 3D beam bunches for the 6D self-consistent phase space distribution in Eq. (2.1), we plan to explore other self-consistent distributions for which the exponent in Eq. (2.1) is different from $-1/2$, such as 1/2 and 3/2. For these other exponents, the equation corresponding to Eq. (2.10) is nonlinear in $G(\boldsymbol{x})$, requiring a numerical solution on a meshlike grid for an elongated bunch. In this way we can see the extent to which our conclusions about halo formation depend on the distribution. We then plan to explore distributions that are not self-consistent, to determine the extent to which the relatively rapid redistribution of the 6D phase space contributes to the formation of halos.

ACKNOWLEDGMENTS

We wish to acknowledge the support of the U.S. Department of Energy, Division of High Energy Physics, and Division of Mathematical, Information, and Computational Sciences. For this research we used resources of the National Energy Research Scientific Computing Center; the research is supported by the U.S. Department of Energy Office of Energy Research. We thank Tom Wangler for helpful conversations. In addition, R.L.G. and A.V.F. wish to thank Andy Jason and the LANSCE1 group for its hospitality during some of these studies.

[1] M. Reiser, in *Proceedings of the 1991 Particle Accelerator Conference*, edited by L. Lizama *et al.* (IEEE, San Francisco, CA, 1991), p. 2497; A. Cucchetti, M. Reiser, and T. Wangler, *ibid.*, p. 251; J. S. O'Connell, T. P. Wangler, R. S. Mills, and K. R. Crandall, in *Proceedings of the 1993 Particle Accelerator Conference*, edited by S. T. Corneliussen (IEEE, Washington, DC, 1993), p. 3657.

[2] R. L. Gluckstern, Phys. Rev. Lett. **73**, 1247 (1994).

[3] M. Reiser, *Theory and Design of Charged Particle Beams* (Wiley, New York 1994).

[4] See I. M. Kapchinsky, *Theory of Resonance Linear Accelerators* (Harwood Academic Publishers, New York, 1985), p. 247ff.

[5] R. L. Gluckstern, W-H. Cheng, S. S. Kurennoy, and H. Ye, Phys. Rev. E **54**, 6788 (1996).

[6] R. L. Gluckstern, W-H. Cheng, and H. Ye, Phys. Rev. Lett. **75**, 2835 (1995).

[7] R. L. Gluckstern and S. S. Kurennoy, in Proceedings of the 1997 Particle Accelerator Conference, Vancouver, Canada (to be published).

[8] J. J. Barnard and S. M. Lund, in Proceedings of the 1997 Particle Accelerator Conference, Vancouver, Canada (to be published); S. M. Lund and J. J. Barnard, *ibid.*

[9] H. Okamoto and M. Ikegami, Phys. Rev. E **55**, 4694 (1997).

[10] R. A. Jameson, in *Frontiers of Accelerator Technology*, edited by S. I. Kurokawa, M. Month, and S. Turner, Proceedings of the Joint US-CERN-Japan Intern'l School, 1994 (World Scientific, Singapore, 1996), pp. 530–560; see also Los Alamos Report No. LA-UR-93-1209.

[11] We take all parameters to be in the Lorentz frame of the bunch, where all motion is nonrelativistic.

[12] APT Conceptual Design Report, Los Alamos Report No. LA-UR-97-1329, 1997.

[13] E. Forest, J. Bengtason, and M. F. Reusch, Phys. Lett. A **158**, 99 (1991).

[14] R. W. Hockney and J. W. Eastwood, *Computer Simulation Using Particles* (Adam Hilger, New York, 1988).

[15] R. Ferrell and E. Bertschinger, Int. J. Mod. Phys. C **5**, 933 (1994).